

**2018 NDIA GROUND VEHICLE SYSTEMS ENGINEERING AND TECHNOLOGY
SYMPOSIUM
MATERIALS & ADVANCED MANUFACTURING TECHNICAL SESSION
AUGUST 7-9, 2018 – Novi, MICHIGAN**

**MICROSTRUCTURAL ANALYSIS AND CREEP BEHAVIOR OF 25MM
THICK FRICTION STIR WELDED AA2139-T8**

Uchechi Okeke

Department of Chemical Engineering &
Materials Science
Michigan State University
East Lansing, MI

Tank Automotive Research,
Development, and Engineering Center
Warren, MI

Carl Boehlert, PhD

Department of Chemical Engineering &
Materials Science
Michigan State University
East Lansing, MI

ABSTRACT

Most studies conducted on friction stir welded (FSW) Al alloys are on plates that are 2.5-7 mm thick. However, the U.S. Army utilizes materials that are 25 mm thick and greater for structure and armor. In order to properly apply FSW to Al-Cu-Mg-Ag alloys for use in next generation ground vehicles, data must be generated and available for model and simulation databases. One key type of data is the tensile-creep behavior of FSW AA 2139-T8. Creep is the time dependent, plastic deformation of a material under a constant load, usually observed at a constant temperature where $T > 0.3T_m$. The objective of this study is to provide information regarding the tensile-creep behavior of the stir zone in comparison to the heat affected zone (HAZ) through the depth of the weld. The results from this research provide information on the effect of FSW processing on the microstructure and creep behavior. Pre- and post-deformation samples were analyzed via SEM and TEM and the results are discussed.

INTRODUCTION AND BACKGROUND

In 1991, The Welding Institute (TWI, UK) developed a solid-state joining technique known as friction stir welding (FSW) [1,2]. This method has been heavily investigated on Al-Cu alloys due to the increased incorporation of Al alloys in the automotive and aerospace industry. FSW of lightweight alloys has shown industrial advantages including the reduction of component weight by eliminating additional joining materials (e.g. rivets,

fasteners, and filler weld), the capability for joining dissimilar materials, and the capability for achieving dimensional restrictions as demonstrated in the 2008 Ford GT application and the NASA Space Shuttle Super-Light Weight Tank [3,4]. Among the several alluring advantages of FSW [5], the primary reason for the invested interest is that it circumvents fusion welding issues on age-hardenable Al alloys, for instance solidification cracking.

FSW requires no additional thermal energy source other than that generated by the friction due to the rotational stirring of the welding tool. In addition, no welding supplemental materials are required. The rotating tool descends with a downward force into the joint of two metal plates which are butted together. The rotating tool traverses along the joint to weld the two plates together. The thermal input and shear deformation result in three unique microstructural zones listed in order from the middle of the weld to the periphery [6]: (i) the stir zone (SZ); (ii) the thermomechanically affected zone (TMAZ); and (iii) the heat affected zone (HAZ). The base metal (BM) region is unaffected by the welding process and maintains its original microstructure and mechanical properties. The mechanical properties, such as hardness and tensile strength, vary across these zones and are strongly dependent on the microstructural changes caused by the heat generation and the stirring [7–10].

Research on FSW has been primarily on Al alloys with thicknesses ranging from 2-7 mm [3,7,10–16] due to private commercial industry interest. This limits the transferable knowledge on the effects of processing on the microstructure and mechanical properties for Al alloys with a thickness of 25 mm and greater. There is also limited information available on the effects of the SZ on the tensile-creep behavior. Creep is the sustained deformation of a material under a constant load and temperature [17]. Due to growing interests and the application of lightweight alloys for automotive and aerospace industries in public and private sectors, elevated temperature loading environments should be investigated. This study aims to provide information on the tensile-creep deformation behavior of thick plate FSW Al-Cu-Mg-Ag alloys at elevated temperatures.

Tensile-creep experiments were conducted on 25 mm thick AA2139-T8. Samples were extracted in the transverse direction parallel to the welding direction in the SZ and the HAZ. This isolation permitted the evaluation of a particular zone. It was

assumed that the microstructure was homogenous through the depth of the SZ. This study, however, demonstrates that tensile-creep behavior through the depth of a single SZ cannot be duplicated due to the varying microstructure. Results were compared to the HAZ samples. In addition, some HAZ samples were extracted and tested in the transverse direction. Electron backscattered diffraction (EBSD), transmission electron microscopy (TEM), and scanning electron microscopy (SEM) were utilized to acquire information on the grain size, precipitation products, and failure behavior. The methodology for material preparation and experimentation are presented in the experimental details section. The pre- and post-test microstructure and creep behavior of the HAZ and SZ are mentioned in the results section and analyzed in the discussion section.

EXPERIMENTAL DETAILS

Material Preparation

Two 76.2 x 45.7 cm plates of wrought, 25 mm thick AA2139-T8 were friction stir welded together by EWI (Columbus, OH) per the welding specifications displayed in Table 1 [8]. The target composition of AA2139 is shown in Table 2. The plates were welded perpendicular to the rolling direction (i.e. in the transverse direction, TD). Samples used for analysis were extracted from the BM, HAZ, and the SZ of this plate in the TD using electrical discharge machining (EDM). The sample dimensions and areas of extraction are depicted in Figure 1. The gage section width and thickness were 12.7 mm and 1.78 mm, respectively. Using SiC grinding paper, the samples were ground prior to testing to both remove the EDM contamination layer and provide a smooth surface.

The nomenclature of samples machined from the SZ was used to record their location through the depth of the weld. Samples used for creep testing were machined from the SZ Bottom, Mid Bottom, and Middle regions as shown in Figure 2. The SZ Bottom samples were machined 0 to 4.2 mm from

the weld root, the very bottom of the weld. The SZ Mid Bottom samples were machined 4.2 to 10.5 mm from the weld root. The SZ Middle samples were machined 10.5 to 14.8 mm from the weld root.

Table 1: Welding parameters.

Parameter	Specification
Shoulder Diameter	41.3 mm
Pin Length	24.7 mm
Plunge Depth	0.51-0.13 mm
Spindle Speed	150-250 RPM
Travel Speed	5.1 CPM
Total Length	45.7 mm

Table 2: Target composition in wt% of AA2139 as listed in The Teal Sheets [18].

Al	Cu	Mg	Ag	Mn	Zn
Bal	4.5-	0.2-	0.15-	0.2-	0.25
	5.5	0.8	0.6	0.6	

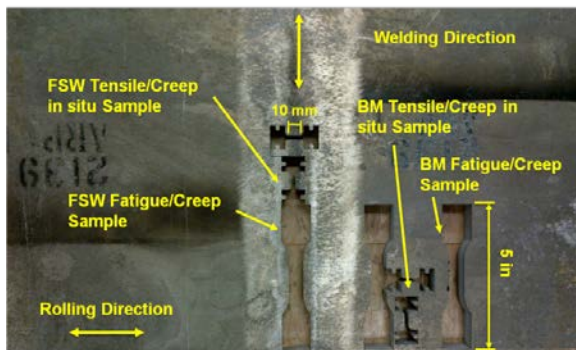


Figure 1: Image depicting how the mechanical test samples were extracted from the welded plates.

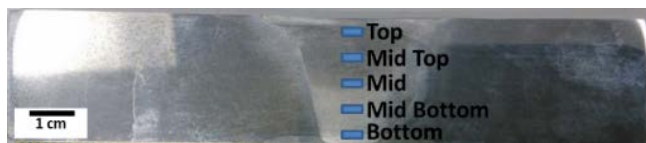


Figure 2: Low magnification image showing the location of 5 areas through the stir zone.

Microscopic Analysis

Images of the fracture surface and the transverse cross section of the samples were acquired using a field emission gun TESCAN Mira3 SEM at a beam voltage of 25kV. Samples sectioned for fractography were cut approximately 1 cm from both fracture surfaces. One side was left to analyze the fracture surface and the other side was mounted to analyze the sample surface at the fracture site. Images were acquired under secondary electron (SE) and backscattered electron (BSE) conditions. EBSD Orientation image maps were acquired and processed with an EDAX (Mahwah, NJ) EBSD detector and TSL OIM software. TEM analysis on the as-welded SZ and deformed samples was performed on a JEOL 2100F. For the untested BM, a JEOL JEM-ARM200F TEM was used. A voltage of 200kV was used for both TEMs. The precipitate volume percent, V_p , was measured using the ImageJ software.

Tensile Testing

Tensile tests were conducted on the large, rectangular dogbone samples, see Figure 1, using a MTS® servo-hydraulic, thermomechanical testing machine with a MTS® Flex Test SE controller (Eden Prairie, MN). The tensile specimens had a thickness of approximately 0.75 mm. The loading axis was parallel to the TD, see Figure 1. The tests were performed at RT at a constant displacement rate of $0.025 \text{ mm}\cdot\text{s}^{-1}$, which corresponded to a strain rate of approximately 10^{-3} s^{-1} . An alumina rod extensometer was used to measure the strain. Engineering stress (σ), 0.02% offset yield strength (YS), elastic modulus (E), and the ultimate tensile strength (UTS) were measured for each experiment.

Creep Testing

Tensile-creep experiments were performed at stresses ranging from 25 to 125 MPa and at temperatures ranging from 225°C to 275°C, see Table 3. The tests were conducted on lever-arm creep machines. Data was recorded using

LabVIEW® VI software. All tests were conducted using two general steps: heat up and creep loading. During the heat up procedure, the temperature was increased to the target temperature within an hour. A load between 3-8 MPa was applied to prevent compression of the sample during heat up. When the target temperature was achieved, the samples were heat soaked for approximately 15 minutes before applying the creep load. The time, temperature, load, and displacement were recorded throughout the test.

slightly rotated and show some texture. The measured average grain size was 32, 8, and 3 μm for the top, middle, and bottom, respectively.



Figure 3: EBSD orientation map of the HAZ in the transverse cross section.

Table 3: List of creep experiments performed.

Region	Temp (°C)	Stress (MPa)
HAZ	250-275	50
Mid-Bottom-1	250-275	50
HAZ	225	50-75-100
Mid-Bottom-2	225	50-75
Bottom	250	25-35-50
Mid-Bottom-3	250	25-35-50

RESULTS

Microstructure

The HAZ microstructure, depicted in the EBSD orientation map in Figure 3, has elongated grains retained from the rolling during the T8 temper. Micrographs through the center of the SZ capture the microstructure from the top of the weld to the bottom in Figure 4. The grain size decreased from the top of the weld, where the average grain size was 30 μm, to the bottom of the weld, where the average grain size was 6 μm. The precipitate volume percent, V_p , had an inverse relationship with the grain size. The lowest V_p was observed at the top (2.4%) while the highest was observed at the bottom (10.6%).

EBSD was performed on the surface normal to the weld at the top, middle, and bottom. The middle is defined as the region in the middle of the plate and the top sample was extracted 8 mm above it. The bottom sample was 8 mm below the middle sample. The EBSD images are presented in Figure 5. The grains at the bottom of the sample in the SZ were

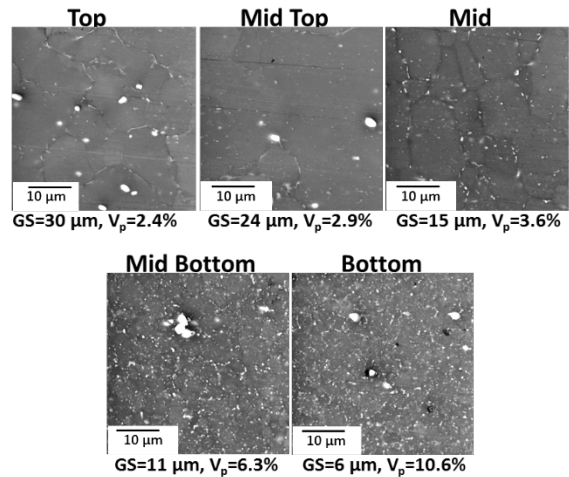


Figure 4: SEM micrographs through the depth of the SZ in the transverse cross section with the measured average grain sizes (GS) and precipitate volume percent (V_p).

Creep of HAZ and SZ

Room temperature (RT) tensile tests were conducted on the BM and SZ in the transverse direction to measure the yield strength, which was used to determine the applied creep stresses. The UTS and the YS for the SZ were both lower than those of the BM, see Figure 6. The BM exhibited a YS, UTS, and elongation to failure of 300 MPa, 433 MPa, and 7.2%, respectively. The SZ exhibited values of 265 MPa, 364 MPa, and 7.3% for the YS, UTS, and elongation to failure, respectively. The E for BM and SZ were 76.6 GPa and 61.1 GPa, respectively.

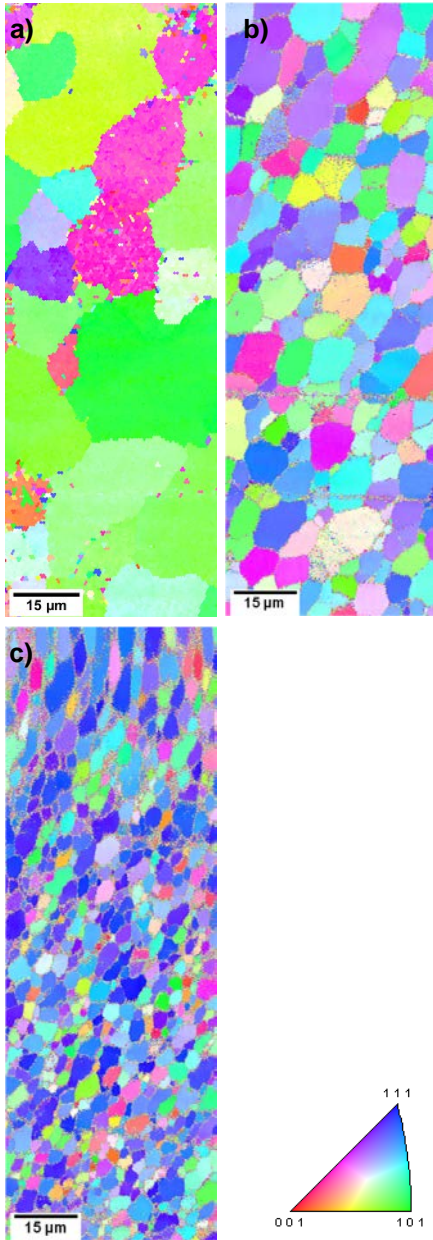


Figure 5: EBSD orientation map of the normal surface of the SZ region at the a) top (average grain size = 32 μm), b) middle (average grain size = 8 μm), and the c) bottom (average grain size = 3 μm).

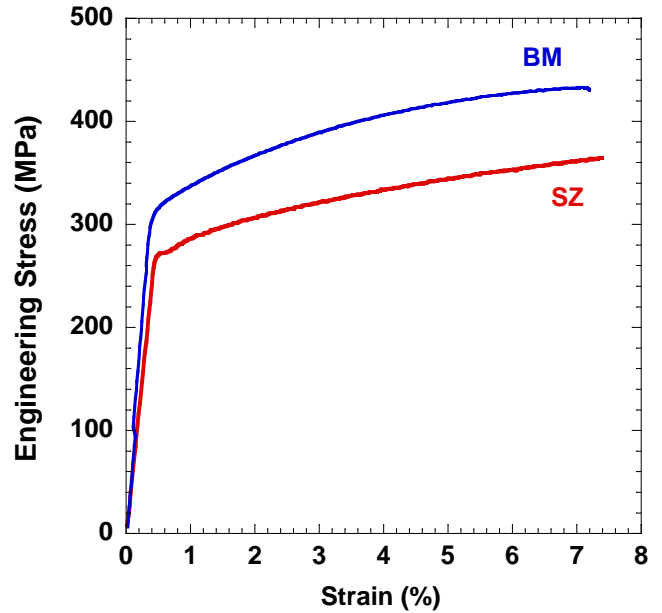


Figure 6: Room temperature stress versus strain curves for the SZ and the BM in the transverse direction.

The stress or temperature was increased after the creep rate versus time plot indicated that a secondary creep stage was reached. In Figure 7 and Figure 8, the creep strain versus time plot of the HAZ was compared to that of the SZ. Figure 7 shows a stress increase test for the HAZ and SZ Mid Bottom-2. The applied stresses ranged from 50-125 MPa in increments of 25 MPa. Samples were tested at a constant temperature of 225°C. SZ Mid Bottom-2 failed after the stress increase to 75 MPa and approximately 350 hrs of testing. The HAZ sample failed after the stress increase to 125 MPa and approximately 700 hrs of testing. The secondary creep rates for SZ Mid Bottom-2 were faster than the HAZ by approximately one order of magnitude. The transverse cross section of the SZ Mid Bottom-2 in Figure 7b shows a refined, equiaxed microstructure with some coarsened precipitates at the grain boundaries. The V_p , Table 4, was 3.5%, which was approximately half that of FSW SZ Mid Bottom-2 (6.3%). Analysis of the SZ Mid Bottom-2 fracture surface in Figure 9 revealed dimples towards the lateral ends of the gage section which is indicative of a ductile fracture. The center

exhibited intergranular features which is indicative of a brittle fracture. The post-test microstructure of the HAZ exhibited intragranular and intergranular precipitate coarsening, as seen in Figure 7c. The precipitate V_p was measured to be 4.3% which was approximately twice that of the untested BM (2.1%). The fracture surface of the HAZ exhibited ductile and brittle features, as well. In Figure 10, the right side of the fracture surface exhibited intergranular cracking and the left side exhibited dimples. The fracture features for both samples were consistent with the elongation-to-failure even though brittle fracture features were observed. A similar observation was noted in the temperature increase experiments.

The SZ Mid Bottom-1 and HAZ were tested at temperatures of 250°C and 275°C at an applied stress of 50 MPa, see Figure 8a. The SZ Mid Bottom sample failed after the temperature increase to 275°C and approximately 200 hrs of testing. The HAZ sample failed after the temperature increase to 275°C and approximately 320 hrs of testing. The transverse cross section of the HAZ in Figure 8c shows intergranular and intragranular precipitate coarsening. The precipitate V_p was 3.8% which was greater than the precipitate V_p of the BM. The transverse cross section of SZ Mid Bottom-1 in Figure 8b reveals a refined, equiaxed microstructure with intergranular and intragranular coarsened precipitates. The precipitate V_p was 7.3%, which was greater than the precipitate V_p of the FSW SZ Mid Bottom-1, see Table 4. Dimples were observed on the lateral sides of the SZ Mid Bottom-1 fracture surface which suggests a ductile fracture and is consistent with the elongation-to-failure; however, brittle fracture features were observed. The center of the sample demonstrated intergranular fracture, see Figure 11.

Creep through the SZ Depth

Two SZ samples were tested at a temperature of 250°C and at applied stresses of 25, 35, and 50 MPa. Although both samples were from the SZ,

they exhibited different creep behavior, as see Figure 12a.

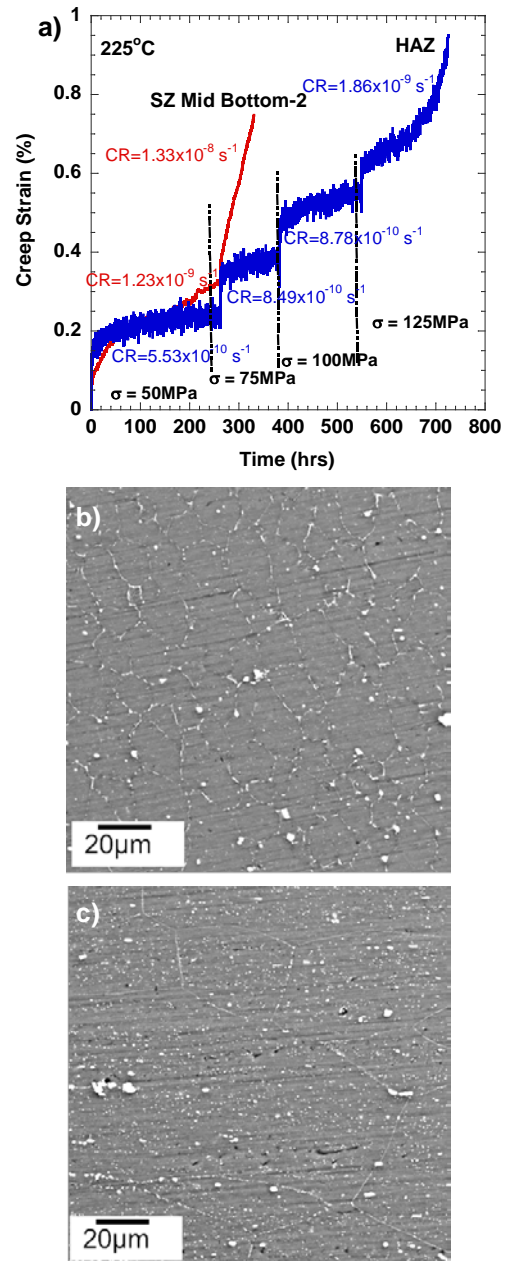


Figure 7: Stress increase test. Creep strain versus time plot for SZ Mid Bottom-2 and HAZ samples at 225°C and stresses ranging between 50-75-100-125 MPa. Micrographs for a) SZ Mid Bottom-2 (0.75% creep strain) and b) HAZ (0.95% creep strain).

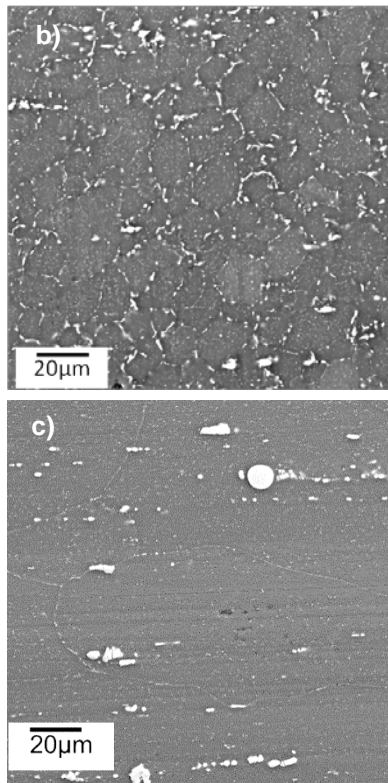
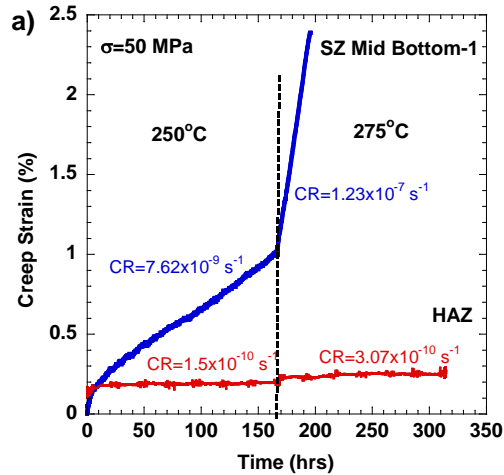


Figure 8: Temperature increase test. a) Creep strain versus time plot for SZ and HAZ samples at temperatures ranging between 250-275°C and at stress of 50 MPa. b) SZ Mid Bottom-1 micrograph (2.4% creep strain). c) HAZ micrograph (0.25% creep strain).

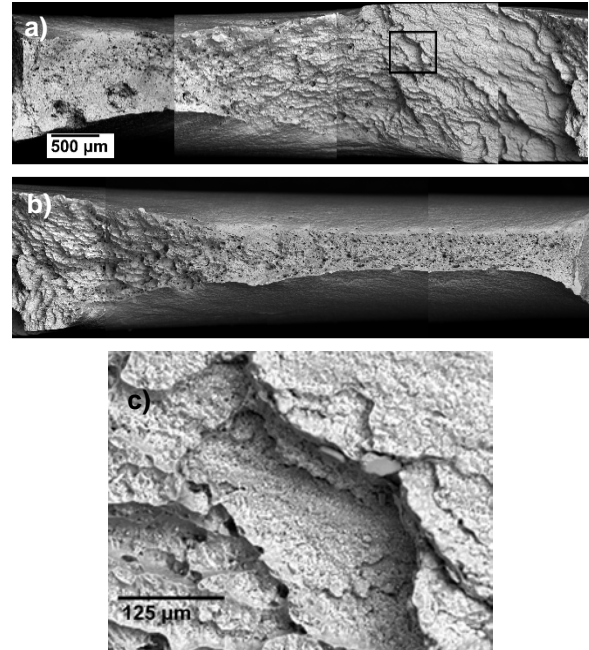


Figure 9: a-b) Fractograph of sample SZ Mid Bottom-2 creep tested at 225°C and 50-75 MPa. Lateral sides of the sample have dimples. c) Intergranular features were observed at the center. Creep strain to failure was 0.75%.

Table 4: Precipitate V_p of the creep tested samples and the center of the SZ through the depth of the weld.

Sample	Stress (MPa)	Temp. (°C)	V_p (%)
SZ Mid Bottom-2	50-75	225	3.5
HAZ	50-75-100-125	225	4.3
SZ Bottom	25-35-50	250	12.5
SZ Mid Bottom-3	25-35-50	250	11.3
HAZ	50	250-275	3.8
SZ Mid Bottom-1	50	250-275	7.2
BM	--	--	2.1
FSW SZ Top	--	--	2.4
FSW SZ Mid Top	--	--	2.9
FSW SZ Mid	--	--	3.6
FSW SZ Mid Bottom	--	--	6.3
FSW SZ Bottom	--	--	10.6

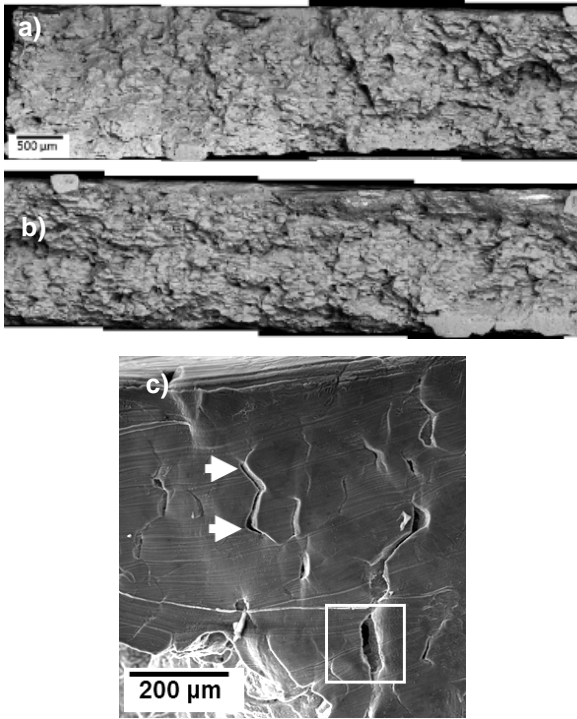


Figure 10: Fractograph of the HAZ creep tested at 225°C and 50-125 MPa. a) Left half contains dimples. b) Right half consists of intergranular cracking. c) Cracking at triple junctions (arrows) and along grain boundaries (boxed area). Creep strain to failure was 0.95%.

The observed maximum creep strain for SZ Bottom at failure was 2.4% at 560 hrs. The creep rates were $2.7 \times 10^{-9} \text{ s}^{-1}$, $1.3 \times 10^{-9} \text{ s}^{-1}$, and $2.1 \times 10^{-8} \text{ s}^{-1}$ for 25, 35, and 50 MPa, respectively. The creep rate did not change significantly when the stress was increased to 35 MPa. Sample SZ Mid Bottom-3 experienced significant increases in creep rate from $7.0 \times 10^{-10} \text{ s}^{-1}$ to $1.1 \times 10^{-8} \text{ s}^{-1}$ to $1.1 \times 10^{-7} \text{ s}^{-1}$ at 25, 35, and 50 MPa, respectively. The observed maximum creep strain at failure was 1.6% after approximately 400 hrs. SZ Bottom had a higher creep strain by almost 0.5% than SZ Mid Bottom-3 at 25 MPa and the creep rate was approximately four times faster. SZ Mid Bottom-3 continued to increase in creep rate at 50 MPa which was greater than SZ Bottom. In general, SZ Bottom exhibited a lower creep rate and higher creep strain values than SZ Mid Bottom-3.

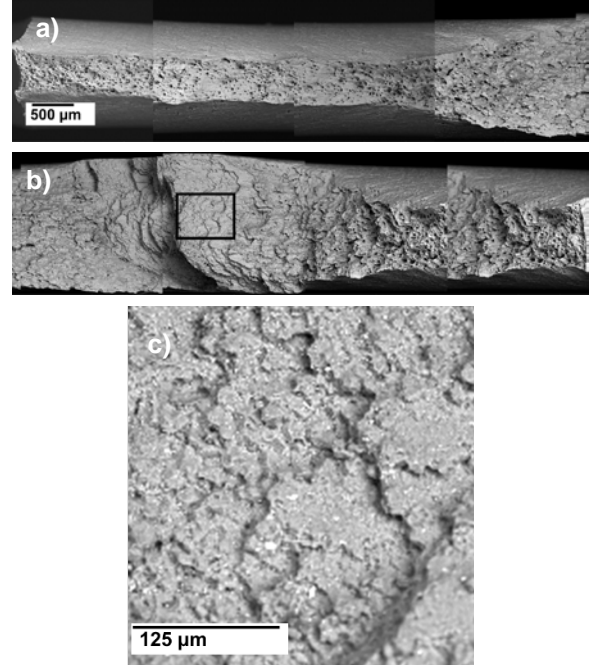


Figure 11: a-b) Fractograph of sample SZ Mid Bottom-1 which underwent a temperature increase creep test at 250-275°C and 50 MPa. c) High magnification of the intergranular fracture of the boxed region in b). Creep strain to failure was 2.4%.

The transverse cross section of SZ Bottom and SZ Mid Bottom-3, see Figure 12b-c, show a refined, equiaxed microstructure with coarsened precipitates, especially at the grain boundaries for both samples. However, SZ Bottom appears to have slightly more precipitate coarsening.

Table 4 and Figure 4 demonstrate that there is a gradient in the microstructure in the SZ. When the precipitate V_p of the two are compared, SZ Bottom and SZ Mid Bottom-3 had higher V_p values (12.5% and 11.3%, respectively) than their corresponding as-welded conditions, bottom and mid-bottom (10.6% and 6.3%, respectively).

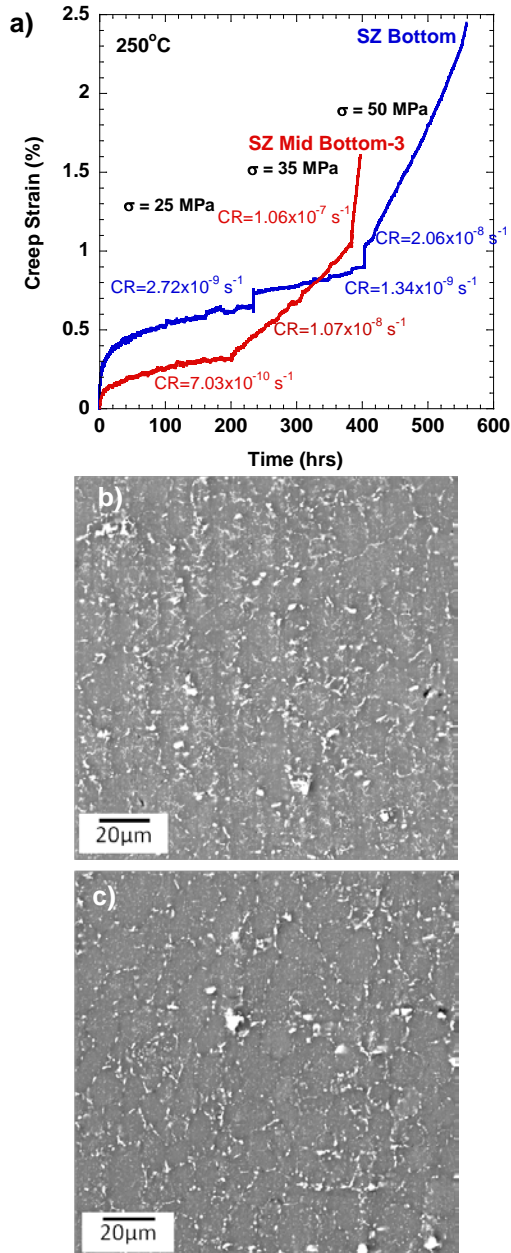


Figure 12: Stress increase test. a) Creep strain versus time plot for SZ samples at 250°C and at stresses ranging between 25-35-50 MPa. Micrographs of b) SZ Bottom (2.4% creep strain) and c) SZ Mid Bottom-3 (1.6% creep strain).

Analysis of the SZ Bottom fracture surface revealed dimples on the left side and dimples on the right half, as seen in Figure 13. Cracks and voids at grain boundaries were observed on the sample

surface. Microvoids are typically a step in the ductile failure process.

The SZ Mid Bottom-3 fracture surface exhibited dimples on the lateral sides, whereas, the center of the fracture exhibited brittle, intergranular cracking, see Figure 14. Figure 12b-c show the SEM image of the post-creep microstructure for SZ Bottom and SZ Mid Bottom-3 samples, which had a refined microstructure and coarsened precipitates.

TEM analysis in Figure 15 shows that SZ Bottom had coarsened θ' and Ω . The dissolution of the Ω phase, the coarsening of the θ' phase, and the precipitation of the σ phase occurred in the SZ Mid Bottom-3.

DISCUSSION

HAZ vs SZ Creep Behavior

The HAZ was more creep resistant than the SZ. This was likely due to the coarse grains which are more favorable for creep resistance than refined grains. In diffusional creep for pure metals, coarser grains have less grain boundary area which makes them less sensitive to diffusion controlled creep processes [19]. It should also be noted that cracks typically form perpendicular to the tensile axis in creep fracture [19]. This occurrence is exacerbated in an equiaxed microstructure [19]. The microstructure of the SZ was both refined and equiaxed which contributed to its poor resistance to creep fracture. Another source of creep resistance in the HAZ was the presence of precipitates as this alloy underwent a T8 temper (solution treatment, cold working, and artificial aging). The BM contains thermally metastable θ' and Ω phases [20,21] as demonstrated in the TEM bright field image in Figure 16. The fine distribution of the thermally metastable, fine particles impede dislocation motion and pin grain boundaries making vacancy generation difficult [19].

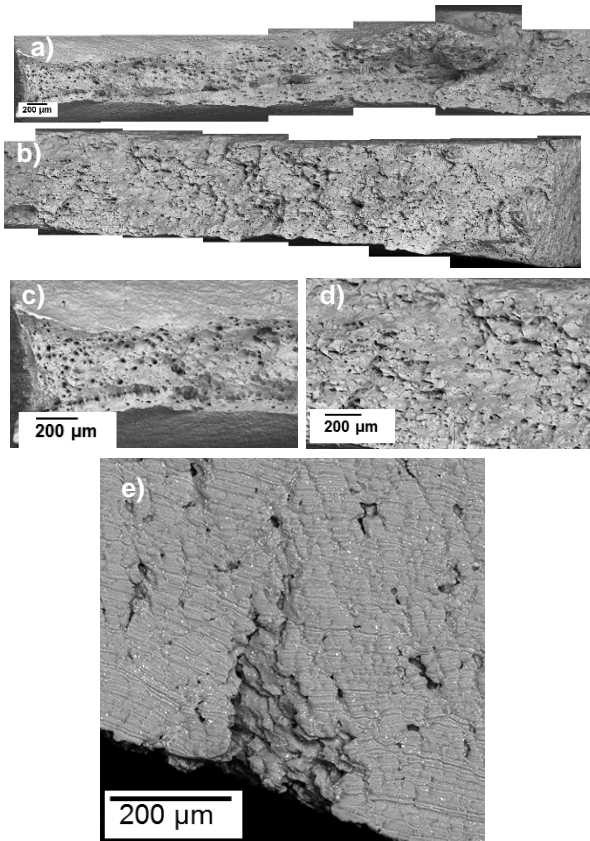


Figure 13: a-b) Fractograph of sample SZ Bottom which underwent a stress increase creep test at 250°C and 25-35-50 MPa. Dimples are present on the fracture surface and are shown in greater detail in c-d). e) Cracks and voids are observed. Creep strain to failure was 2.4%

However, the coarse grains and the presence of fine precipitates should not be interpreted as providing microstructural stability as both the SZ and HAZ exhibited instabilities which manifested as precipitate coarsening. Another phase was detected in the creep tested HAZ sample. Based on the TEM image in Figure 17, this additional phase is most likely the σ phase. It was reported in Mondolfo's Al alloy reference book [21], as having a chemical composition of $Al_5Cu_6Mg_2$, a cubic crystal structure, a cuboid appearance, and it habits the $\{100\}_\alpha$ planes. The significance of this phase on the creep behavior is yet to be determined. After

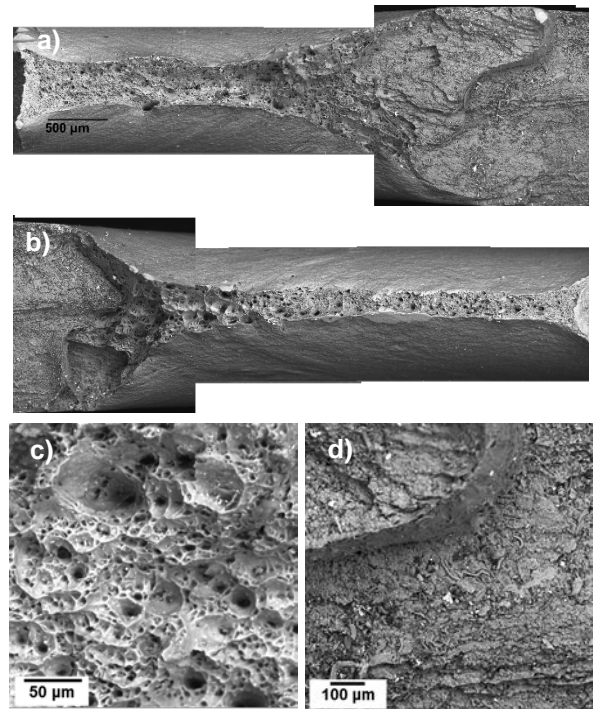


Figure 14: a-b) Fractograph of SZ Mid Bottom-3 creep tested at 250°C and 25-35-50 MPa. Lateral sides have dimples shown in c). The center contains evidence of intergranular fracture shown in d). Creep strain to failure was 1.6%.

the stress increase experiment, the Ω phase dissolved and the σ phase precipitated in the HAZ. There was no expectation to detect the σ -phase due to the limited information of it occurring during testing at temperatures above 200°C and at loads below 100 MPa [22].

The stress increase SZ sample, SZ Mid Bottom-2, was extracted from the mid-bottom area of the as-welded SZ. The V_p was less than that of the as-welded Mid Bottom which is also evident when both transverse cross section micrographs are compared. This was in contrast to the other SZ samples which had higher V_p than their corresponding as-welded region. It is possible that precipitate dissolution occurred, however, more analysis is needed to confirm this.

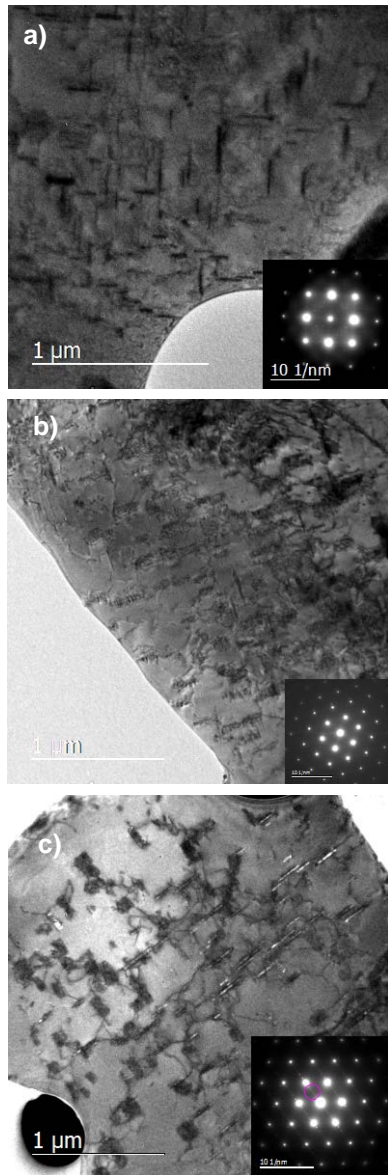


Figure 15: a-b) Bright field micrograph in the $\langle 100 \rangle$ and $\langle 110 \rangle$ zone axes of SZ Bottom and c) SZ Mid Bottom-3 in the $\langle 110 \rangle$ (bottom) creep tested at a temperature of 250°C and stresses of 25-35-50 MPa.

According to the micrograph and diffraction pattern in Figure 18, the as-welded SZ at Mid-Bottom only contained the coarsened Ω phase. Figure 19 illustrates that during the stress increase creep test, the Ω phase coarsened. This is indicated by the transition of the $\langle 111 \rangle$ streaks in the $\langle 110 \rangle$ zone axis in Figure 16 into dots; this is evident of a

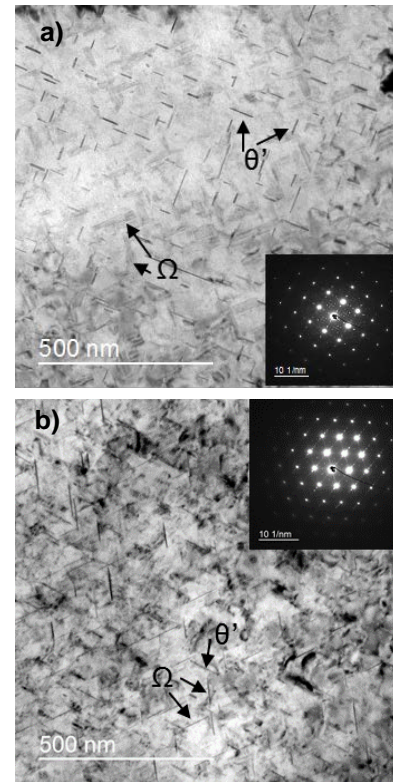


Figure 16: Bright field TEM micrograph of the a) $\langle 100 \rangle$ and the b) $\langle 110 \rangle$ (right) zone axes with the respective inset diffraction patterns.

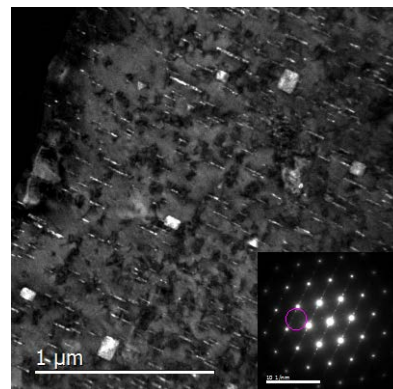


Figure 17: Dark field micrograph in the $\langle 110 \rangle$ zone axis of the HAZ creep tested at a temperature of 225°C and stresses of 50-125 MPa showing the θ' and σ (cuboidal) phases.

change in precipitate shape, or in this case, the precipitate platelet orientation to the electron beam [23]. Some of the θ' orientation variants have precipitated during the creep test as they were not present in the as-welded condition.

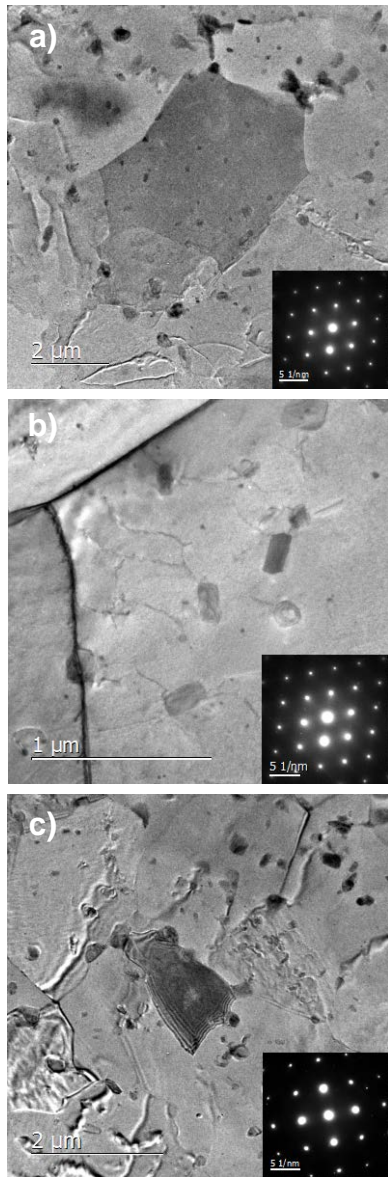


Figure 18: Bright field TEM micrographs. a-b) Mid-bottom SZ in the $\langle 110 \rangle$ zone axis with coarsened θ' , c) Bottom SZ in the $\langle 100 \rangle$ zone axis.

Microstructure through the SZ depth

Most FSW studies performed on thin sheets of metal fail to report vertical microstructural heterogeneity through the depth of the SZ. Thus, the initial assumption was the SZ depth had a homogenous microstructure. However, the precipitate V_p and the grain size varied through the weld depth. As a result, the SZ creep behavior

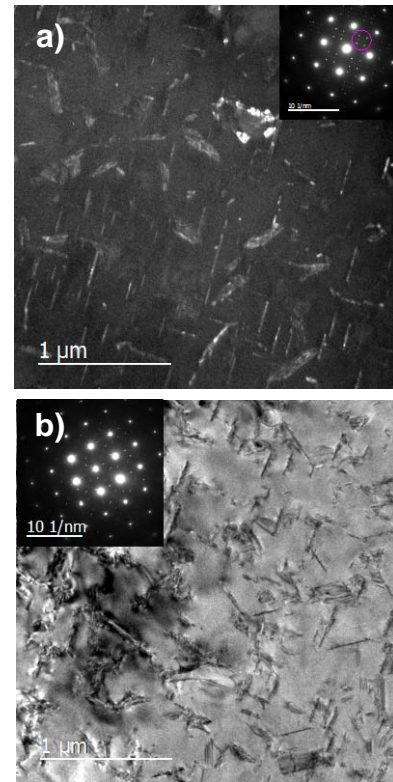


Figure 19: a) Dark field micrograph in the $\langle 100 \rangle$ zone axis and b) bright field micrograph in the $\langle 110 \rangle$ zone axis of SZ Mid Bottom-2 creep tested at a temperature of 225°C and stresses of 50-125 MPa. Stress increases were done in 25 MPa increments. Ω and θ' phases have coarsened.

varied. When compared to values of the correlating areas in Table 4, it is apparent that the precipitates coarsened due to the exposure of the heat from the creep test. This also suggests that the microstructure was evolving during the test and was, therefore, thermally unstable. The bottom sample, SZ Bottom, had a higher V_p than the mid bottom, SZ Mid Bottom-3, which meant that the precipitate growth kinetics was not unstable so that the mid bottom sample, which had a lower precipitate V_p than the bottom sample before creep, did not have a higher precipitate V_p than the bottom sample after creep.

It is probable that the precipitates found on the fracture surfaces contributed to the creep failure as there is increased strain within the grain due to

lattice mismatch with the coarsening precipitates. The gage section of the creep samples only contained the SZ and no HAZ or TMAZ. Thus, the location of a sample through the depth of the SZ could result in a combination of fracture types, brittle and ductile. One possible explanation of this could be found in analyzing the rotation of the grains due to the plastic flow of metal around the FSW tool. The plastic deformation due to FSW causes a dynamically recrystallized microstructure in the SZ. The recrystallized grains were either equiaxed or elongated and seemingly rotated, see Figure 5. More analysis is needed to firmly correlate the fracture type and mechanism to the grain orientation.

The difference in the microstructure led to the difference in the creep performance. This presents an issue as it indicates that when SZ material is exposed to the same temperature and stress, the rate of deformation will vary through the weld. This limits the application of SZ in environments with prolonged elevated temperatures under sustained loading. Although testing conditions for SZ Mid Bottom-2 and SZ Mid Bottom-3, which were extracted right next to each other, were different, the 25°C difference led to very distinct microstructures in which SZ Mid Bottom-3 precipitated the σ phase and SZ Mid Bottom-2 experienced precipitate coarsening of the θ' and Ω phases.

SUMMARY

The FSW process results in a significantly finer, equiaxed grain size in the SZ compared to the HAZ. In addition, when compared to the HAZ, the SZ samples had higher secondary creep rates and a shorter creep life. The microstructure in the SZ is a function of the thickness through the weld. Consequently, the resulting properties and the deformation and fracture behavior were a function of the microstructure. For thicker Al-Cu-Mg-Ag alloys, it is expected that similar gradients in the microstructure could also result in different creep behavior as a function of the depth in the weld.

ACKNOWLEDGEMENTS

This research was supported by the U.S. National Science Foundation Division of Material Research (Grant No. DMR1107117). Use of the TEMs at the Center for Nanoscale Materials at Argonne National Laboratory, an Office of Science user facility, was supported by the U.S. Department of Energy, Office of Science, Office of Basic Energy Sciences, under Contract No. DE-AC02-06CH11357. Special thanks to Dr. Yuzi Liu, Center of Nanoscale Materials, who was a great assistance in acquiring the as-welded and deformed TEM images. This work was also performed in part at the Institute of Materials Research, Tohoku University through the National Science Foundation East Asia & Pacific Summer Institute Fellowship (Award No. 1515111). The authors are grateful to Dr. Makoto Nagasako and Mr. Shun Ito for acquiring the TEM images.

REFERENCES

- [1] W. M. Thomas, E. D. Nicholas, J. C. Needham, M. G. Murch, P. Temple-Smith, C. J. Dawes, Friction stir butt welding, 9125978–8, 1991.
- [2] W. M. Thomas, E. D. Nicholas, J. C. Needham, M.G. Murch, P. Temple-Smith, C. J. Dawes, Improvements relating to friction welding, 5460317, 1991.
- [3] Matthew Zaluzec, Light-Weight Materials in Automobiles: Designing the Ford Fusion, Past, Present and Future (unpublished research), (2014).
- [4] National Aeronautics and Space Administration, Space Shuttle Technology Summary: Friction Stir Welding, Pub 8-1263. FS-2001-03-60-MSFC (n.d.). http://www.nasa.gov/centers/marshall/pdf/104835main_friction.pdf.
- [5] P.L. Threadgill, A.J. Leonard, H.R. Shercliff, P.J. Withers, Friction stir welding of aluminium alloys, *Int. Mater. Rev.* 54 (2009) 49–93. doi:10.1179/174328009X411136.

- [6] American Welding Society, Specification for Friction Stir Welding of Aluminum Alloys for Aerospace Applications, Stand. D17-3200X. (2006).
- [7] V.T. Saccon, B.S. Parra, C.W. Olea, J.F. dos Santos, N.G. de Alcântara, Microstructural characterization and mechanical behavior of an AA2139 T3 and T8 aluminum alloy joined by friction stir welding (FSW), *Soldag. Amp Insp.* 15 (2010) 289–297. doi:10.1590/S0104-92242010000400006.
- [8] T. Sano, J. Yu, J. Medintz, C.-F. Yen, K. Doherty, The Effect of Friction Stir Welding on the Microstructure and Tensile Properties of Al 2139-T8 Alloys, in: C.E. Suarez (Ed.), *Light Met. 2012*, John Wiley & Sons, Inc., 2012: pp. 497–501. <http://onlinelibrary.wiley.com/doi/10.1002/9781118359259.ch84/summary> (accessed April 4, 2014).
- [9] T. Sano, U. Okeke, J. Yu, C. Boehlert, C.-F. Yen, Tms, Analysis of the Microstructure and Properties of Friction Stir Weld Zones in the Al 2139-T8 Alloy, in: *TMS 2014 Suppl. Proc.*, John Wiley & Sons, Inc., 2014: pp. 545–555. <http://onlinelibrary.wiley.com/doi/10.1002/9781118889879.ch66/summary> (accessed October 30, 2014).
- [10] H.R. Shercliff, M.J. Russell, A. Taylor, T.L. Dickerson, Microstructural modelling in friction stir welding of 2000 series aluminium alloys, *Mech. Ind.* 6 (2005) 25–35. doi:10.1051/meca:2005004.
- [11] D. Alléhaux, F. Marie, Mechanical and Corrosion Behaviour of the 2139 Aluminium-Copper Alloy Welded by the Friction Stir Welding Using the Bobbin Tool Technique, *Mater. Sci. Forum.* 519–521 (2006) 1131–1138. doi:10.4028/www.scientific.net/MSF.519-521.1131.
- [12] A. J. Leonard, in: *Proc 2nd Int Symp ‘Friction Stir Welding,’* TWI, Gothenburg, Sweden, 2000.
- [13] J. Schneider, R. Stromberg, P. Schilling, B. Cao, W. Zhou, J. Morfa, O. Myers, Processing Effects on the Friction Stir Weld Stir Zone, *Weld. J.* 92 (2013) 11–19.
- [14] J. C. Bassett, S. S. Birley, in: *2nd Int Symp Frict. Stir Weld.*, TWI, Gothenburg, Sweden, 2000.
- [15] A.R. Pyzalla, Internal Stresses in Engineering Materials, in: W. Reimers, A.R. Pyzalla, A. K. Schreyer, H. Clemens (Eds.), *Neutrons Synchrotron Radiat. Eng. Mater. Sci. Fundam. Mater. Compon. Charact.*, Wiley-VCH, Weinheim, Germany, 2008: pp. 21–56.
- [16] H. Dai, J.A. Francis, H.J. Stone, H.K.D.H. Bhadeshia, P.J. Withers, *Met Mater Trans A.* 39 (2008) 3070–3078.
- [17] G.E. Dieter, *Mechanical Metallurgy*, 3rd ed., McGraw-Hill, NY, 1986.
- [18] International Alloy Designations and Chemical Composition Limits for Wrought Aluminum and Wrought Aluminum Alloys, in: *Regist. Rec. Ser. Teal Sheets*, The Aluminum Association, 2015.
- [19] R.W. Evans, B. Wilshire, *Introduction to Creep*, The Institute of Materials, London, 1993.
- [20] B. Muddle, I. Polmear, The precipitate Ω phase in Al-Cu-Mg-Ag alloys, *Acta Metall.* 37 (1989) 777–789. doi:10.1016/0001-6160(89)90005-9.
- [21] L.F. Mondolfo, *Aluminum alloys: structure and properties*, Butterworths, London; Boston, 1976.
- [22] R.N. Lumley, I.J. Polmear, The effect of long term creep exposure on the microstructure and properties of an underaged Al-Cu-Mg-Ag alloy, *Scr. Mater.* 50 (2004) 1227–1231. doi:10.1016/j.scriptamat.2004.02.001.

- [23] D.B. Williams, C.B. Carter, Transmission electron microscopy: a textbook for materials science, 2nd ed, Springer, New York, 2008.